# Multi-Segment Magnetic Flux Path Analysis of Wound-Field Flux-Switching Machines with Different Winding and Stator-Rotor Combinations

Mostafa Fereydoonian, *Student Member*, *IEEE*, Dheeraj Bobba, *Member*, *IEEE*, Woongkul Lee, *Senior Member*, *IEEE*

***Abstract*—Wound field flux switching machine (WFFSM) showcases attractive features such as a robust rotor structure, variable field operation capability, and no risk of demagnetization. The WFFSM also provides an integrated stator structure that accommodates both field and armature windings, while the rotor does not require windings or magnets. However, having both windings on the stator creates long and inefficient magnetic flux paths at specific rotor positions that do not directly contribute to electromagnetic torque generation. Therefore, it is imperative for WFFSMs to thoroughly investigate the magnetic flux paths associated with the stator bridge structure. This paper employs a multi-segment magnetic equivalent circuit to identify these longer magnetic flux paths, validated through finite element analysis. In addition, their impact on inductance and torque production of WFFSMs with different winding configurations as well as stator-rotor pole combinations. Torque segregation and energy conversion loop analysis are conducted to visualize and quantify the impact of the longer magnetic flux paths on electromagnetic performances. The study reveals that the inductance harmonics originating from the integrated stator structure generate a negative reluctance torque, decreasing the net output torque. The results demonstrate that the WFFSM employing a circumferential field and armature winding configuration, which does not suffer from the longer magnetic flux path, achieves the highest output torque. It exhibits an output torque 57% higher than the WFFSMs suffering from the longer magnetic flux path, with identical volume.**

***Index Terms*—energy conversion loop, flux-switching, inductance, magnetic equivalent circuit, magnetic flux linkage, permeability, toroidal winding, torque segregation, wound field.**

## I. INTRODUCTION

In recent years, externally excited synchronous machines (EESMs) have attracted attention in the passenger car sector. Their appeal lies in their ability to eliminate rare earth magnets from their design and their high efficiency at low torque and high-speed conditions [1]-[3]. This efficiency enhancement is particularly valuable for improving vehicle range during highway driving, a crucial factor in customer satisfaction. WFFSM, a type of EESM, features all excitation sources located on the stator, while the rotor carries neither windings nor magnets [4], [5]. This design eliminates the need for brushes and slip rings, as illustrated in Fig. 1. The WFFSMs possess robust rotor structure, low cost, effective thermal management capability, fault tolerance, and easy flux regulation [6]-[8]. However, both field and armature windings coexist in the stator, leading to a complex and inefficient magnetic flux path generation [9]-[11]. The integrated stator structure of WFFSMs results in significant leakage flux under highly saturated operating conditions. The root cause of this leakage and the longer magnetic flux path has not been well investigated and understood. Hence, this paper aims to close this knowledge gap by studying the magnetic flux path of WFFSMs with several field and armature winding and stator-rotor pole combinations, using a multi-segment magnetic equivalent circuit (MEC) and FEA validated by multiple methods such as inductance analysis, torque segregation, and energy conversion loop.

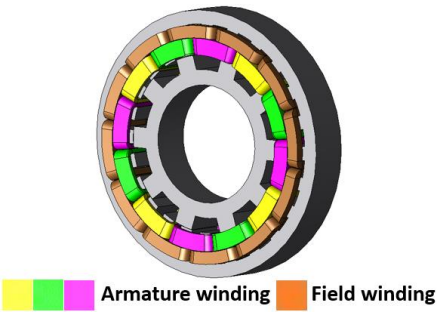

Fig. 1. WFFSM with 12/10 stator-rotor pole combination in 3D.

Magnetic flux path analysis is an effective way to study the flux linkage and interaction between field and armature windings [12]-[14]. FEA-based magnetic flux path analysis was carried out for different rotor positions in [14] to study the electromagnetic performance of WFFSMs. MEC has been known as an effective means for modeling flux density distribution in flux switching machines (FSMs) [15]-[21]. The outcomes demonstrate a good agreement among FEA, MEC, and experimental results. The research conducted in [22] indicates that the torque segregation method serves as a reliable approach for examining how the rotor and stator structure influence the electromagnetic performance of electric machines. The energy conversion loop technique provides the required visual tools to understand the performance and parameters of WFFSMs [23]. The research presented in [24]-[26] exclusively focused on optimizing field and armature winding topologies with a 12/10 combination. The studies in [27]-[30] exclusively focused on one type of field and armature winding topologies with different stator-rotor pole combinations. However, the effect of longer magnetic flux path originating from the integrated stator structure leading to substantial leakage flux in WFFSM has not been investigated in detail for all feasible winding topologies in the previous literature. The MEC is effective in flux path analysis study;

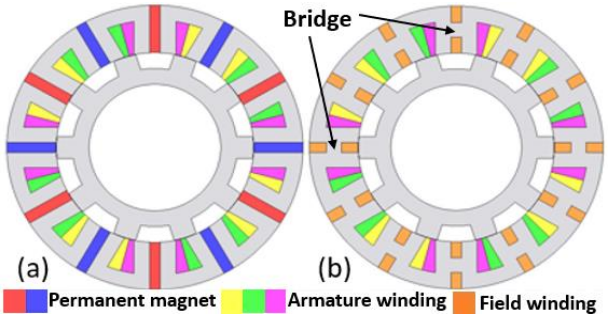


Fig. 2. Cross section of 12/10 (a) FSPMM and (b) WFFSM with the bridge between stator poles.

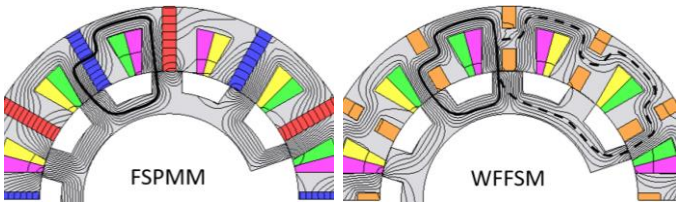


Fig. 3. Magnetic flux line for 12/10 FSPMM and WFFSM.

however, the conventional MEC, widely used in FSM, does not provide a full rotational analysis nor the longer magnetic flux path extending to multiple segments [15]-[21]. Therefore, this paper leverages a new MEC analysis that includes multi-segment MEC and analytically proves the existence of longer magnetic flux path in WFFSM in specific rotor positions with selected stator-rotor pole combinations. Furthermore, previous studies covered only one type of winding topology for several or single stator-rotor pole combinations. WFFSMs with different stator-rotor pole combinations are commonly seen in previous works, but the different winding topologies have still not been investigated comprehensively.

This paper aims to close this knowledge gap by studying the magnetic flux path of WFFSMs with four different types of field and armature winding configurations, along with all four feasible stator-rotor pole combinations. It employs a multi-segment MEC and FEA approach validated through various methods, including inductance analysis, torque segregation, and energy conversion loop analysis. This comprehensive methodology extends beyond the capabilities of experimental studies, encompassing four different winding configurations and all possible stator-rotor pole combinations. Rather than focusing solely on prototyping specific WFFSM types, this study utilizes multi-segment MEC and FEA methods to offer novel and deep insights into the magnetic flux path of FSPMM and WFFSMs with four different winding configurations and four stator-rotor pole combinations. This paper will focus on analytical and simulation methods to validate key observations, aligning with methodologies used by other researchers. The paper aims to visually and quantitatively illustrate the impact of longer magnetic flux paths by conducting inductance analysis, torque segregation, and energy conversion loop analysis. By pinpointing the issue of longer magnetic flux paths, this study can contribute to a deeper understanding of WFFSM performance and pave the road for optimization studies to improve the electromagnetic performance of WFFSM, such as output torque and efficiency.

TABLE 1. CLASSIFICATION OF WFFSMS.

| Winding | Type A | Type B | Type C | Type D |
|---|---|---|---|---|
| **Field** | TW | TW | CW | CW |
| **Armature** | CW | TW | CW | TW |

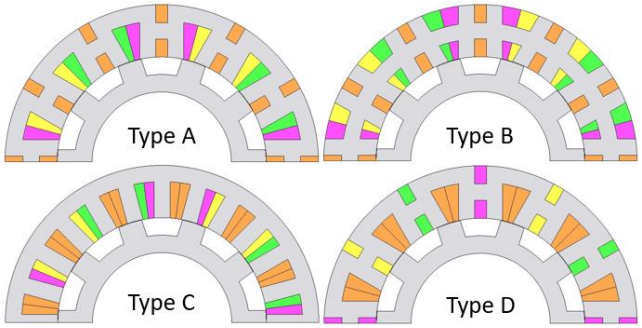


Fig. 4. Cross-section of the WFFSMs with four different feasible winding topologies.

## II. MAGNETIC EQUIVALENT CIRCUIT FOR FLUX PATH ANALYSIS OF FSPMM AND WFFSM WITH DIFFERENT WINDING CONFIGURATION

The FSPMM has a "U" shape modular stator structure, and permanent magnets (PMs) act as a flux barrier (large air-gap) between two adjacent stator modules, as shown in Fig. 2. These flux barriers prevent the magnetic flux from leaking to the pole after the adjacent stator and rotor poles. However, in WFFSM, the stator structures are not modular but connected through the bridges. In fact, replacing the PMs with field windings creates a soft magnetic flux path between two adjacent stator poles. The FSPMM produces all flux paths enclosed through two adjacent stator and rotor poles, as indicated by the solid black line in Fig. 3. However, the integrated stator structure in WFFSM can lead to an additional longer magnetic flux path between phases, indicated with dashed black lines. This undesirable longer magnetic flux path generates localized saturation regions in the stator back iron and the bridges, increases armature winding self- and mutual inductances, and decreases output torque [9].

### *A. WFFSM Winding Configuration*

There are two possible winding topologies, i.e., toroidal winding (TW) and circumferential winding (CW) for the field and armature windings. Accordingly, it generates a two-by-two matrix combination for WFFSMs [10], as summarized in Table 1. Therefore, there are four major types of WFFSMs: Type A, Type B, Type C, and Type D, as shown in Fig. 4. The conventional WFFSM (Type A) has a toroidal field winding and circumferential armature winding. The armature winding can also be toroidal rather than circumferential. In this case, the armature winding is also wound around the stator yoke instead of the stator pole (Type B). This type of stator winding has the advantages of short end-winding, no winding overlap, and is relatively easy to manufacture with a higher fill factor. It also provides better cooling because the stator windings are directly exposed to the stator housing with a cooling jacket [31], [32]. In Type C, both field and armature are CW. Lastly, field and armature are CW and TW in Type D, respectively. The initial investigation indicates that type D does not produce a sinusoidal

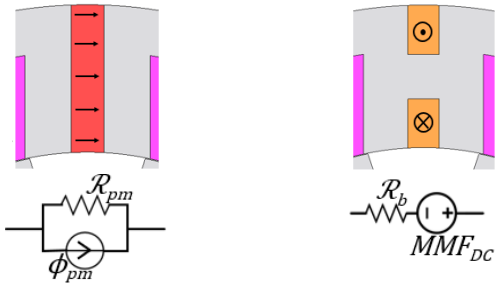


Fig. 5. MEC model of excitation systems in FSPMM and WFFSM.

back-emf. As a result, this particular machine is excluded from further consideration within this study.

### B. Categorization of MEC Elements

The multi-segment MEC method is based on the analogies of the quantity relations in a magnetic field and a resistive electric circuit, as shown in (1).

$$\phi = {}^{\mathcal{F}}/_{\mathcal{R}} = \mathcal{F}\,\rho \tag{1}$$

In which $\varphi$ is the flux, $\mathcal{F}$ is the magnetomotive force (MMF), $\mathcal{R}$ is the reluctance, and $\rho$ is the permeance.

Multi-segment MEC consists of two categories of elements: passive elements as reluctance and active elements as sources. Sources can be further classified into MMF and flux sources. Usually, In MEC, the current-carrying coils are modeled as MMF sources because Ampere's law can easily determine their MMF. PM is another active element, acts as a source, and can be modeled as an MMF source with reluctance in series or flux sources with reluctance in parallel, as shown in Fig. 5. Black arrows indicate the magnetization direction for the magnet. Circles with a dot or a cross indicate the direction of the field current in the machine. In the FSPMM under study, the magnets and armature winding flux are parallel, and the influence of armature reaction field on the working point of magnets is almost eliminated [17], [19]. As a result, the flux density variation in the magnets is small. Thus, in this paper, PMs are represented by a flux source parallel with a linear resistance. Based on the definition of a DC current source, the current is stiff and unchangeable, while in voltage sources, the current could be altered depending on the circuit conditions.

A stator multi-segment MEC module is defined as the MEC model that represents the magnetic flux path distribution in a unit section of the stator, i.e., the section between the central axes of each two neighboring stator slots. The rotor multi-segment MEC modules are obtained by dividing the rotor into equal sections, each with a rotor tooth in the middle. The stator and rotor modules for FSPMM and WFFSMs in a simplified rectilinear arrangement are shown in Fig. 6. The PMs in FSPMM are modeled as DC current source parallel with a resistance, the field coils in the WFFSM Type A are modeled as a DC voltage source series with a resistance, and finally, the armature winding in both machines are modeled as an AC voltage source series with a resistance. The symbols in Fig. 6 are defined in the following equations:

$$\phi_{pm} = B_r A_{pm} \tag{2}$$
$$MMF_{DC} = N_{DC} I_{DC} \tag{3}$$

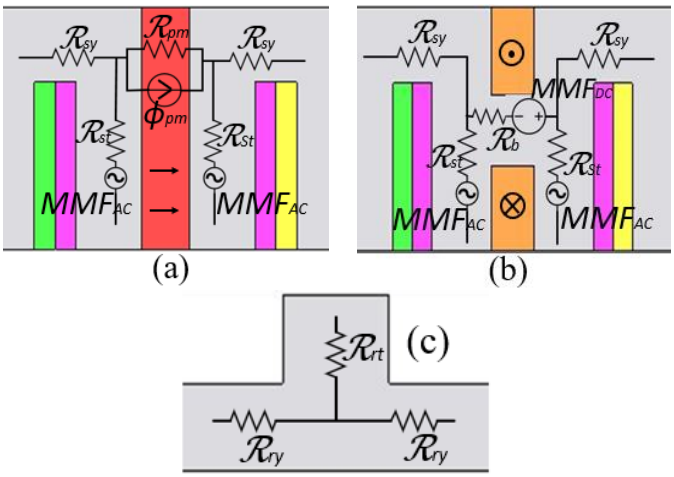


Fig. 6. A single-segment of MEC modules of (a) FSPMM stator, (b) WFFSM stator, and (c) rotor for both machines.

$$MMF_{AC} = N_{AC} I_{AC} \tag{4}$$
$$\mathcal{R} = \int_l {}^{1}/_{\mu A}\, dl \tag{5}$$

PM reluctance is much higher than bridge structure reluctance because PM acts as an air-gap while bridge structures are made of soft magnetic material.

### C. Magnetic Equivalent Circuit and Flux Path Analysis

This subsection analyzes the magnetic behavior of PMs and the bridge structure, focusing on the interaction between the MMF generated by the armature winding currents and both types of excitation systems. Specific rotor positions are selected for all machines, as depicted in Fig. 7. The figure displays the magnetic flux lines, the direction of the winding currents, and the direction of the PM flux. Excitations are applied, with a DC current density of 8.5 A/mm$^2$ injected into the WFFSM and an AC current density of 8.5 A/mm$^2$ aligned with the q-axis injected into the armature windings of both machines. It should be noted that, at this specific rotor position, the current vector of the armature winding corresponds to a positive peak value in the phase W windings and half of this current magnitude in the opposite direction in both the phase U and V windings. The multi-segment MEC model of FSPMM and WFFSMs for this specific rotor position are shown in Fig. 8, and the circuit parameters are summarized in Table 2. By applying Kirchhoff's voltage law (KVL) to the circuit, the magnetic fluxes for both MEC circuits are calculated as follows. According to KVL for the FSPMM:

$$\begin{aligned} &MMF_v + MMF_w - \varphi_1(\mathcal{R}_{sy} + \mathcal{R}_{st} + \mathcal{R}_{gap} + \mathcal{R}_{rt} + \mathcal{R}_{ry}) \\ &-(\varphi_1+\varphi_2)(\mathcal{R}_{rt} + \mathcal{R}_{gap} + \mathcal{R}_{st}) - (\varphi_1 - \phi_{pm})\mathcal{R}_{pm} = 0 \end{aligned} \tag{6}$$

$$\begin{aligned} &MMF_w + MMF_u - (\varphi_2 + \varphi_1)(\mathcal{R}_{st} + \mathcal{R}_{gap} + \mathcal{R}_{rt}) \\ &-\varphi_2(\mathcal{R}_{sy} + \mathcal{R}_{ry}) - (\varphi_2 - \varphi_3)(\mathcal{R}_{st} + \mathcal{R}_{gap} + \mathcal{R}_{rt}) \\ &-(\varphi_2 - \phi_{pm})\mathcal{R}_{pm} - (\varphi_2 + \phi_{pm})\mathcal{R}_{pm} = 0 \end{aligned} \tag{7}$$

$$MMF_v - MMF_u - (\varphi_3 - \varphi_2)(\mathcal{R}_{st} + \mathcal{R}_{gap} + \mathcal{R}_{rt})$$

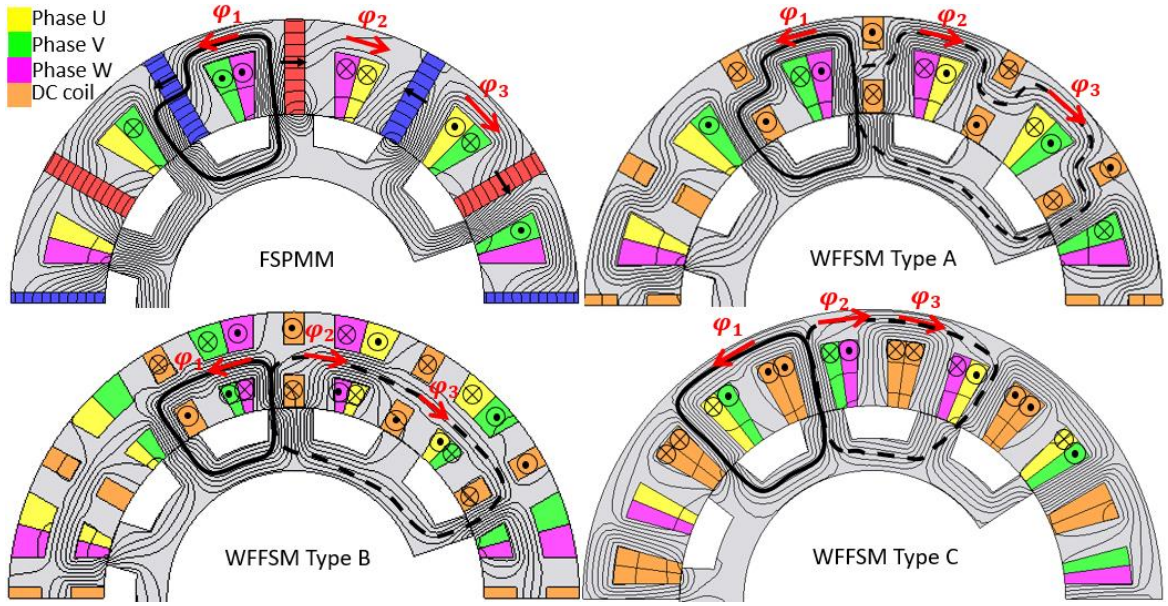


Fig. 7. Magnetic flux line for the FSPMM and WFFSMs at rated condition (rated armature current and excitation).

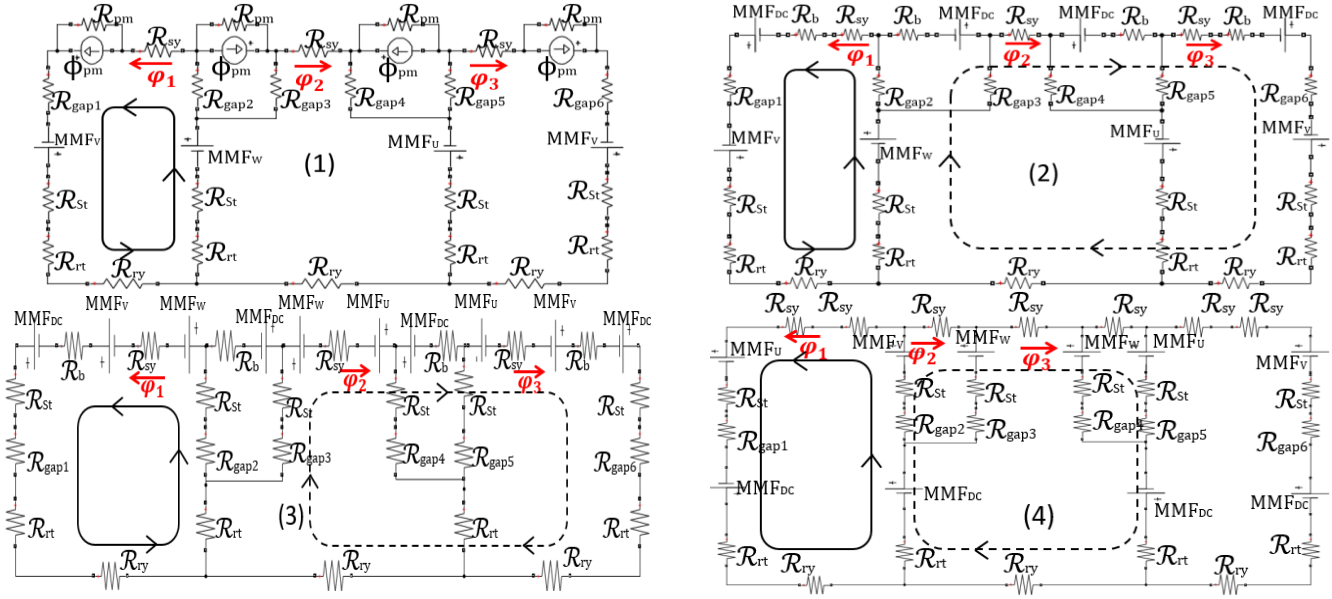


Fig. 8. Multi-segment MEC of (1) FSPMM and WFFSMs, (2) Type A, (3) Type B, and (4) Type C.

$$-\varphi_3(\mathcal{R}_{sy}+\mathcal{R}_{st}+\mathcal{R}_{gap}+\mathcal{R}_{rt}+\mathcal{R}_{ry})$$

$$-(\varphi_3-\phi_{pm})\mathcal{R}_{pm}=0 \tag{8}$$

KVL for the WFFSM Type A:

$$MMF_w+MMF_{DC}+MMF_v-\varphi_1(\mathcal{R}_{sy}+\mathcal{R}_b+\mathcal{R}_{st}+\mathcal{R}_{gap}$$
$$+\mathcal{R}_{rt}+\mathcal{R}_{ry})-(\varphi_1+\varphi_2)(\mathcal{R}_{rt}+\mathcal{R}_{gap}+\mathcal{R}_{st})=0 \tag{9}$$

$$MMF_w+MMF_{DC}-MMF_{DC}+MMF_u-\varphi_2(\mathcal{R}_{sy}+\mathcal{R}_b+\mathcal{R}_{ry}$$
$$+\mathcal{R}_b)-(\varphi_2+\varphi_1)(\mathcal{R}_{st}+\mathcal{R}_{gap}+\mathcal{R}_{rt})-(\varphi_2-\varphi_3)(\mathcal{R}_{st}$$
$$+\mathcal{R}_{gap}+\mathcal{R}_{rt})=0 \tag{10}$$

$$MMF_v-MMF_u+MMF_{DC}-\varphi_3(\mathcal{R}_{sy}+\mathcal{R}_b+\mathcal{R}_{st}+\mathcal{R}_{gap}$$
$$+\mathcal{R}_{rt}+\mathcal{R}_{ry})-(\varphi_3-\varphi_2)(\mathcal{R}_{rt}+\mathcal{R}_{gap}+\mathcal{R}_{st})=0 \tag{11}$$

The FEA results and multi-segment MEC analysis results for all machines are summarized in Table 3. The magnetic flux in the middle loop ($\varphi_2$) in FSPMM MEC is relatively small (0.3 mWb) compared with that of WFFSM (2.75 mWb). The significant flux paths are highlighted with lines in all MECs of Fig. 8. For the FSPMM, the flux $\varphi_1$ flows through the left loop because the $MMF_V$ and $MMF_W$ augment the PM flux source.

The presence of the flux source $\phi_{pm}$ in parallel with high reluctance $\mathcal{R}_{pm}$ in the middle loop results in a relatively diminished flux $\varphi_2$ within said loop. However, For the WFFSMs MEC circuit, alongside the flux in the left loop, indicated with a solid line, the phase *MMF*s and DC *MMF*s with the same direction augment and overcome the $MMF_{DC}$ in the opposite direction, consequently creating a longer magnetic flux path in a bigger loop, indicated with a dashed line. This longer path magnetic flux linkage increases the self- and mutual inductances in WFFSM. This phenomenon is not observed for

TABLE 1. MEC PARAMETERS IN FSPMM AND WFFSM.

| MEC Parameter | | Unit |
|---|---|---|
| $\mathscr{R}_{pm}$ | PM reluctance | $H^{-1}$ |
| $\mathscr{R}_{b}$ | Bridge structure reluctance | $H^{-1}$ |
| $\mathscr{R}_{sy}$ | Stator back iron reluctance | $H^{-1}$ |
| $\mathscr{R}_{st}$ | Stator tooth reluctance | $H^{-1}$ |
| $\mathscr{R}_{ry}$ | Rotor back iron reluctance | $H^{-1}$ |
| $\mathscr{R}_{rt}$ | Rotor tooth reluctance | $H^{-1}$ |
| $\mathscr{R}_{gap}$ | Air-gap reluctance | $H^{-1}$ |
| $\phi_{pm}$ | PM main flux | Wb |
| $MMF_u$ | MMF due to current in phase U coil | At |
| $MMF_v$ | MMF due to current in phase V coil | At |
| $MMF_w$ | MMF due to current in phase W coil | At |
| $MMF_{DC}$ | MMF due to current in DC coil | At |

TABLE 3. COMPARISON OF MAGNETIC FLUX IN FSPMM AND WFFSMS.

| Method / Machine | Magnetic Flux [mWb] | FEA | MEC | Error [%] |
|---|---|---|---|---|
| **FSPMM** | $\boldsymbol{\varphi_1}$ | 2.88 | 3 | 4.1 |
| | $\boldsymbol{\varphi_2}$ | 0.3 | 0.3 | 0 |
| | $\boldsymbol{\varphi_3}$ | 2.64 | 2.63 | 0.3 |
| **Type A** | $\boldsymbol{\varphi_1}$ | 3.4 | 3.46 | 1.7 |
| | $\boldsymbol{\varphi_2}$ | 2.87 | 2.75 | 4.1 |
| | $\boldsymbol{\varphi_3}$ | 1.76 | 1.73 | 1.7 |
| **Type B** | $\boldsymbol{\varphi_1}$ | 4 | 4 | 0 |
| | $\boldsymbol{\varphi_2}$ | 4 | 3.9 | 2.5 |
| | $\boldsymbol{\varphi_3}$ | 1.86 | 1.9 | 2.1 |
| **Type C** | $\boldsymbol{\varphi_1}$ | 3.83 | 3.9 | 1.8 |
| | $\boldsymbol{\varphi_2}$ | 1 | 1 | 0 |
| | $\boldsymbol{\varphi_3}$ | 3.83 | 3.8 | 0.7 |

the FSPMM. The disparity in magnetic flux values between the multi-segment MEC and FEA methods is attributed to the simplification inherent in the multi-segment MEC model. This multi-segment MEC model neglects the influence of leakage flux and the impact of other coils.

The multi-segment MEC and FEA methods show that for WFFSM Type A, for each phase during an electric cycle at four specific rotor positions, the armature winding reaction changes the direction of the magnetic flux in the bridge structure and creates a longer magnetic flux path, enclosing through the pole after the adjacent stator and rotor pole. The net result is that the flux production of PM in FSPMM is not adversely affected by the presence of armature current. Because the armature current MMF contributes to PM flux sources. Nevertheless, for the WFFSM armature, current MMF has a significant effect on DC coil flux, and at four rotor positions, the flux direction of the bridge structure changes.

## III. ANALYTICAL TORQUE ESTIMATION CONSIDERING THE EFFECT OF LONGER MAGNETIC FLUX

The electromagnetic torque, $T_e$, developed in electric machines generally consists of two components, a reluctance torque ($T_{rel}$) and an excitation torque ($T_{exc}$), and can be expressed as:

$$T_e = T_{rel} + T_{exc} = \frac{1}{2}\sum_n i_n^2 \frac{dL_{nn}}{d\theta} + \frac{1}{2}\sum_k \sum_m i_k i_m \frac{dM_{km}}{d\theta}, \quad k \neq m, \quad n,k,and\ m \in \{u,v,w,f\} \tag{12}$$

TABLE 4. FSMS SPECIFICATION.

| Parameter | Units | Value | |
|---|---|---|---|
| | | FSPMM | WFFSM |
| **Rated power** | kW | 300 | 300 |
| **Rated speed** | rpm | 4,000 | 4,000 |
| **Number of stator-rotor pole** | - | 12/10 | 12/10 |
| **$J_{AC}$ and $J_{DC}$ (armature and field current density)** | A/mm$^2$ | 8.5 | 8.5 |
| **DC field excitation** | - | SmCo | Field winding |
| **$N_{dc}$ (turns per dc coil)** | - | - | 4 |
| **$N_{ac}$ (turns per coil per phase)** | - | 3 | 3 |
| **Stator / Rotor outer diameter** | mm | 540 / 359 | 540 / 359 |
| **Stator / Rotor tooth width** | mm | 28 / 42 | 28 / 42 |
| **Filling factor** | - | 0.5 | 0.5 |
| **Air-gap ($l_g$)** | mm | 0.5 | 0.5 |
| **Stack length** | mm | 80 | 80 |
| **Cooling** | - | Liquid cooling jacket [32] | |

where $L_{nn}$ is all windings self-inductance, $M_{mk}$ is the mutual inductance, $i_n$ is armature and field currents, and $\Theta$ is the electrical angular position of the rotor. As the operation of the FSM with sinusoidal current is with the current placed in phase with the back-emf, the primary torque production is coming from $T_{exc}$ and can be expressed as:

$$T_{exc} = \sum_k \sum_m e_k(t) i_m(t), \qquad m \neq k \tag{13}$$

Using (13), (12) can be written as follows:

$$T_e = T_{rel} + T_{exc} = \frac{1}{2}\sum_n i_n^2 \frac{dL_{nn}}{d\theta} + \sum_k \sum_m e_k(t) i_m(t). \tag{14}$$

In general, for FSMs, the topology of the stator and rotor is designed and arranged to produce torque entirely as an excitation torque component, and the contribution of $T_{rel}$ is negligible [33], [34]. In this study, the back-emf ($e_k(t)$) of the FSPMM and WFFSM Type A are comparable (164 V and 151 V, respectively) and the armature currents ($i_m(t)$) are identical and in phase with the back-emf. Therefore, based on (13), the excitation torque ($T_{exc}$) generated by both machines is comparable. Therefore, it is expected that both machines will show comparable net output torque. However, the net output torque of FSPMM (908 Nm) is about twice that of WFFSM Type A (450 Nm). This means that the WFFSM Type A generates a negative reluctance torque ($T_{rel}$), which decreases this machine net output torque. Inductance analysis and torque segregation are conducted to explore this phenomenon further.

### A. Self- and Mutual Inductances Waveforms

Generally, FSMs are designed to operate in a saturated condition to obtain a high flux density in the air-gap. Therefore, FSMs inductance calculations are greatly affected by the nonlinear magnetic behavior and cross-coupling effect [35]. Due to the double saliency and parallel magnetic circuit of the FSMs, armature winding inductance $L$ ($\Theta$, $i$) depends on both rotor position and armature current [36]. In the literature [37]-[39], there are several definitions for inductances, depending on their mathematical description; the most common definitions

are static and incremental inductances. The incremental inductance ($L = d\lambda/di$) rather than the static inductance ($L = \lambda/i$) is required to predict the dynamic behavior and performance of electromagnetic systems with saturation.

The incremental inductance formula efficiently calculates the armature winding inductance since it can incorporate saturation and cross-coupling effects. It can be expressed as follows:

$$L_{mn} = \frac{d\lambda_m}{di_n} \approx \frac{\Delta\lambda_m}{\Delta i_n} = \frac{\lambda_{m2} - \lambda_{m1}}{i_{n2} - i_{n1}} \tag{15}$$

The FEA tool and (15) are used to measure the armature self- and mutual inductances in the stator frame, shown in Fig. 9. Type A and B exhibit considerable spikes (200% for self-inductance and 400% for mutual inductance). Type C has an inductance waveform similar to the FSPMM, except that it has more harmonic due to more saturation in the stator yoke. Table 5 summarizes the average and rms inductance values in stator frames. The WFFSM Type A and Type B exhibit elevated average self- and mutual inductance, attributed to the spikes in the inductance waveforms. The FSPMM shows the lowest average self and mutual inductances.

In contrast, Type A and B show high average self and mutual inductance due to the spikes in the inductance waveforms and their roots in the presence of bridges between the stator poles and the longer magnetic flux path. The longer magnetic flux path increases self- and mutual inductances in WFFSMs. In all FSMs, the average value of mutual inductance is almost half that of self-inductance due to the special machine topologies.

It is reported in [40] that the self-inductances of FSMs armature winding vary as a periodic function of the electrical angle of the rotor position $\Theta$. The self-inductance of each phase has even and odd harmonic components, and odd harmonic components cancel out each other. Therefore, self-inductance can be written as:

$$\begin{aligned} L_{uu} &= \sum_{n=0} L_n \cos 2n\theta, \\ L_{vv} &= \sum_{n=0} L_n \cos 2n(\theta - \frac{2\pi}{3}), \\ L_{ww} &= \sum_{n=0} L_n \cos 2n(\theta + \frac{2\pi}{3}), \\ & n = 0, 1, 2, \ldots \end{aligned} \tag{16}$$

For the FSPMM, by neglecting higher even harmonics:

$$\begin{aligned} L_{uu} &= 16.8 + 3.6\cos 2\theta \ \ \mu\text{H}, \\ L_{vv} &= 16.8 + 3.6\cos 2\left(\theta - \frac{2\pi}{3}\right) \mu\text{H}, \\ L_{ww} &= 16.8 + 3.6\cos 2\left(\theta + \frac{2\pi}{3}\right) \mu\text{H}. \end{aligned} \tag{17}$$

From (14), the reluctance torque $T_{rel}$ generated by the FSPMM can be calculated:

$$T_{rel} = \frac{1}{2} i_u^2 \frac{dL_{uu}}{d\theta} + \frac{1}{2} i_v^2 \frac{dL_{vv}}{d\theta} + \frac{1}{2} i_w^2 \frac{dL_{ww}}{d\theta} \tag{18}$$

$$T_{rel} = \frac{1}{2} i_m^2 sin^2(\theta)(-2L_2 \sin 2\theta)$$

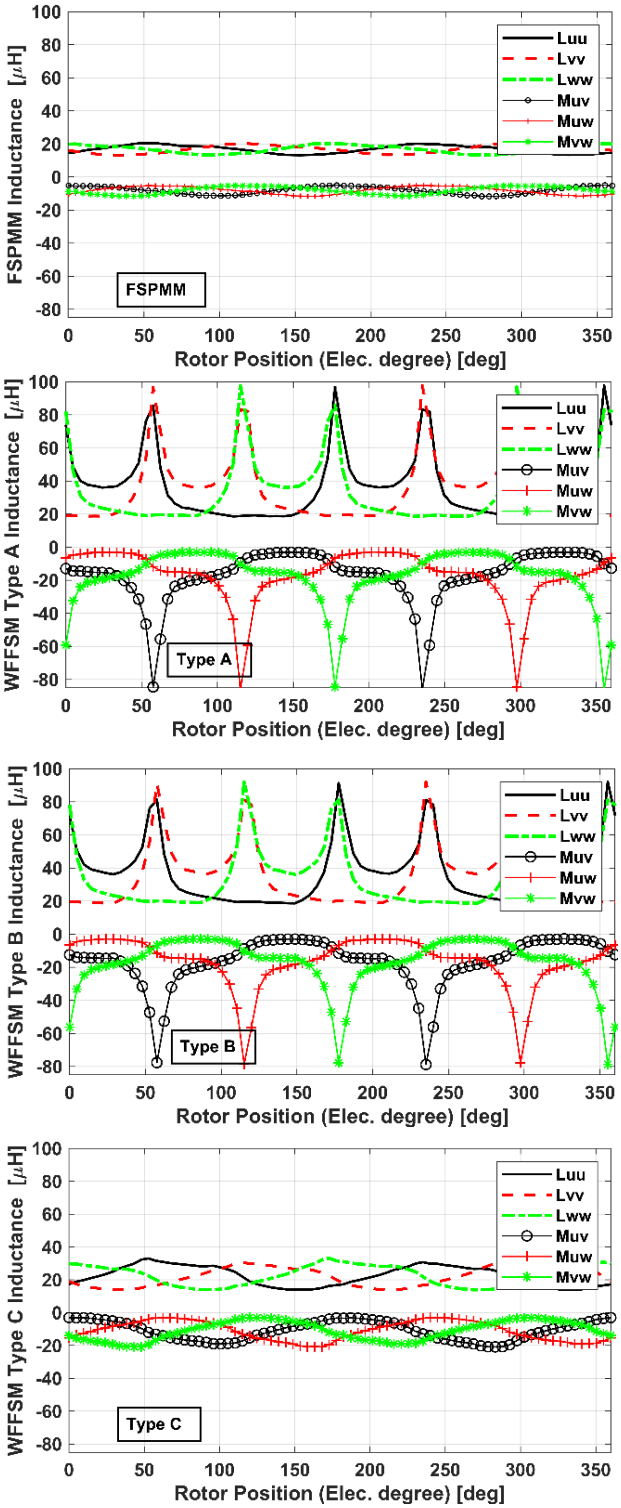


Fig. 9. FSPMM and WFFSMs armature winding inductance waveforms in stator frame.

Table 5. FSPMM AND WFFSMS SELF- AND MUTUAL INDUCTANCES IN STATOR FRAME

| Machine | Armature winding self-inductances (average) [μH] | | | Armature winding mutual inductances (average) [μH] | | |
|---|---|---|---|---|---|---|
| | $L_{uu}$ | $L_{vv}$ | $L_{ww}$ | $M_{uv}$ | $M_{uw}$ | $M_{vw}$ |
| **FSPMM** | 16.81 | 16.83 | 16.81 | 8.04 | 8.02 | 8.3 |
| **Type A** | 35.17 | 35.16 | 35.17 | 17.16 | 17.24 | 17.6 |
| **Type B** | 35.55 | 35.55 | 35.55 | 16.73 | 16.86 | 16.75 |
| **Type C** | 22.41 | 22.41 | 22.42 | 10.94 | 10.93 | 10.94 |

$$+\frac{1}{2}\ i_m^2 sin^2\left(\theta-\frac{2\pi}{3}\right)(-2L_2\sin 2(\theta-\frac{2\pi}{3}))$$
$$+\frac{1}{2}\ i_m^2 sin^2\left(\theta+\frac{2\pi}{3}\right)\left(-2L_2\sin 2(\theta+\frac{2\pi}{3}\right) \quad (19)$$

$$T_{rel} = -\ i_m^2 L_2[sin^2\theta\sin 2\theta$$
$$+sin^2\left(\theta-\frac{2\pi}{3}\right)\sin 2\left(\theta-\frac{2\pi}{3}\right)$$
$$+sin^2\left(\theta+\frac{2\pi}{3}\right)\sin 2\left(\theta+\frac{2\pi}{3}\right)] = 0 \quad (20)$$

This implies that the average reluctance torque produced by an ideal FSPMM is zero. However, in the case of the WFFSMs, the armature winding self-inductances ($L_{uu}$, $L_{vv}$, and $L_{ww}$) exhibit a noteworthy presence of both odd and even harmonics:

$$L_{uu} = \sum_{n=0} L_n \cos n\theta,$$
$$L_{vv} = \sum_{n=0} L_n \cos n(\theta-\frac{2\pi}{3}),$$
$$L_{ww} = \sum_{n=0} L_n \cos n(\theta+\frac{2\pi}{3}),$$
$$n = 0, 1, 2, \ldots \quad (21)$$

The reluctance torque generated by WFFSMs is:

$$T_{rel} = \frac{1}{2}\ i_u^2\frac{dL_{uu}}{d\theta} + \frac{1}{2}\ i_v^2\frac{dL_{vv}}{d\theta}$$
$$+\frac{1}{2}i_w^2\frac{dL_{ww}}{d\theta} + \frac{1}{2}\ I_f^2\frac{dL_f}{d\theta} \quad (22)$$

As shown in (20) the reluctance torque generated by even harmonics of $L_{uu}$, $L_{vv}$, and $L_{ww}$ is zero; however, the odd harmonics of $L_{uu}$, $L_{vv}$, and $L_{ww}$ result in a non-zero negative reluctance torque. The final element in (22) represents the reluctance torque resulting from alterations in the inductance of the field winding; here $L_f$ and $I_f$ stand for field winding inductance and field current, respectively. This reluctance torque with a net-zero value is, in fact, the cogging torque. As derived from equations (20)-(22), the reluctance torque arising from even harmonics within the armature winding self-inductances of WFFSMs sums up to zero. However, its odd harmonic components result in a negative reluctance torque.

### *B. Torque Segregation*

There are analytical methods to segregate the excitation and reluctance torques by (12) and obtain the inductances. However, because of the nonlinear characteristics of materials and highly uneven magnetic flux density and permeability distribution in each part of FSMs, it is difficult to segregate the torques mathematically. Therefore, the FEA-based frozen permeability method is used to segregate the torque components. The torque components of both the FSPMM and the WFFSM Type A, including excitation torque, reluctance torque, and net output torque, are plotted as functions of the armature current angle in Fig. 10. The plot provides a visual representation of the variations in torque components for different armature current angles. The FSPMM shows a relatively small negative reluctance torque (10% of excitation torque) at zero armature current angle that comes from odd harmonics of self-inductance. However, for WFFSM Type A, negative reluctance torque (38% of excitation torque) is generated at zero current angle. This significant negative reluctance torque arising from a substantial presence of self-inductance odd harmonics adversely affects the torque capability of the machine. The FSPMM exhibits an excitation torque of 1,000 Nm, which is higher than that of the WFFSM Type A, 739 Nm. This difference is attributed to the higher back-emf of the FSPMM. The back-emf of the FSPMM and WFFSM Type A is 164 V and 151 V, respectively. The higher back-emf leads to more powerful electromagnetic forces, thus causing a greater excitation torque in the FSPMM than the WFFSM Type A.

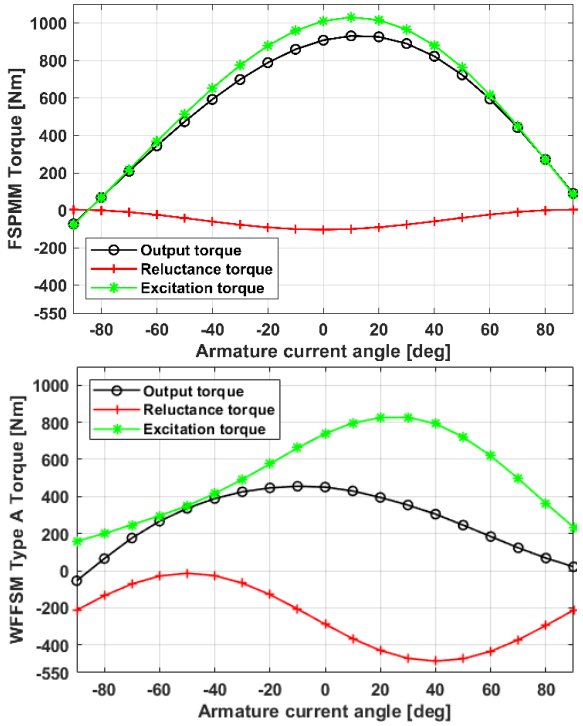

Fig. 10. Torque segregation for the FSPMM and the WFFSM Type A.

The major finding of this section is the longer magnetic flux path contributed by the bridge structure generates a significant amount of odd harmonics in self-inductances that adversely affect the electromagnetic performance of WFFSM Type A.

## IV. Effect of the Longer Magnetic Flux Path in Different Types of WFFSMs

### *A. Electromagnetic performance*

The terminal voltage waveform and the corresponding back-emf waveform of the FSMs under investigation are depicted in Fig. 11. The FSPMM and WFFSMs Type A, Type B, and Type C show sinusoidal back-emf waveform with rms values of 164 V, 151 V, 152 V, and 130 V, respectively. However, Type A and Type B terminal voltage shows four spikes for an electric cycle. This means that during an electric cycle, four specific rotor positions create a longer magnetic flux path, leading to a steep change in the armature winding flux linkage, producing

four spikes in the terminal voltage waveforms.

The instantaneous torque waveforms are compared in Fig. 12. The FSPMM and WFFSMs Type A, Type B, and Type C have an average torque of 908 Nm, 450 Nm, 455 Nm, and 707 Nm, respectively. As explored in the previous section, replacing PMs with DC coils creates an integrated stator structure. It leads to a negative reluctance torque. Among all WFFSMs, Type C, which does not suffer from the longer magnetic flux path, achieves the highest output torque of 707 Nm. Specifically, it exhibits a torque that is 57% higher compared to Type A and Type B, which suffer from the longer magnetic flux path. The output torque, cogging torque, torque ripple, and efficiency are summarized in Table 6. Due to the stator and rotor saliency, flux-switching machines tend to have relatively high cogging torque. Type C shows the highest peak-to-peak cogging torque, 89 N.m. Cogging torque reduction can be obtained by skewing and rotor tooth optimization methods. Type C has the lowest torque ripple of 8.88% at rated load. Due to the switching of flux linkages in the rotor, the rotor iron loss of FSMs is more significant than that of the regular synchronous machines, which will degrade the efficiency of FSMs [41]. In the constant torque region, the FSPMM exhibits superior efficiency compared to the WFFSMs.

### *B. Energy Conversion Loop*

The energy conversion loop analysis is conducted to visualize and quantify the impact of the longer magnetic flux path. The armature flux linkage and current ($\lambda$-$i_a$) characteristics are chosen to plot the energy conversion loops. The area of the energy conversion loop is proportional to the change of magnetic energy inside the machine and, consequently, output torque [23]. The energy conversion loop for all FSMs at rated conditions is plotted in Fig. 13. Each energy conversion loop corresponds to one phase flux linkage variation over one electrical cycle at rated current density. The FSPMM loop has an elliptic shape and covers the widest area. Type A and B similarly exhibit distorted narrower loops, even though the armature flux linkage reaches a relatively high flux linkage of 0.075 Wb (even higher than that of FSPMM). It means in these machines, by increasing armature current $i_a$, the flux linkage $\lambda$ also increases up to 0.075 Wb; however, unlike the FSPMM, the energy conversion loop area does not increase significantly. This indicates that the inefficient longer magnetic flux leaking through the bridge adversely affects the motor performance, and the higher armature current does not increase output power/torque. Type A and B have almost identical energy conversion loops, and both suffer from the longer magnetic flux path. Type C has an elliptic loop similar to the FSPMM.

### *C. WFFSMs with Different Stator-Rotor Pole Combinations*

The study in [42] shows that the optimized rotor pole number should be close to that of stator poles. Furthermore, to obtain balanced symmetrical back-emf in three-phase all-slot-wound FSMs, condition (23) has to be satisfied:

$$\frac{N_s}{GCD(N_s, N_r)} = 6K, \quad K \in N \tag{23}$$

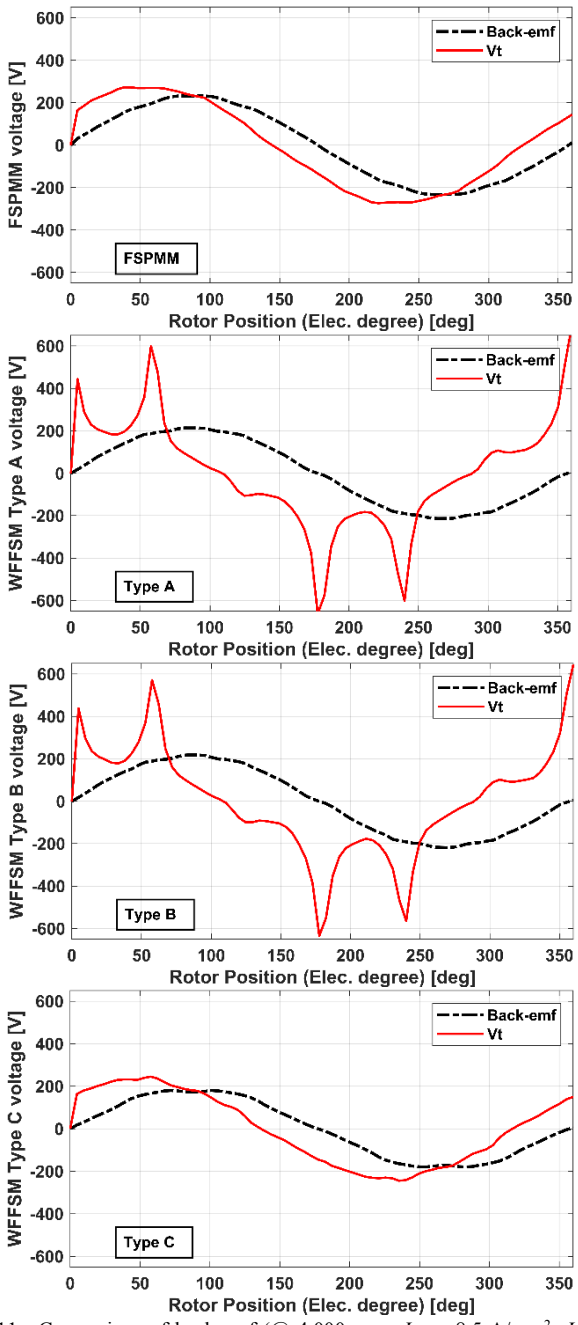


Fig. 11. Comparison of back-emf (@ 4,000 rpm, $J_{DC}$ = 8.5 A/mm$^2$, $J_{AC}$ = 0 A/mm$^2$) and terminal voltage (@ 4,000 rpm, $J_{DC}$ = 8.5 A/mm$^2$, $J_{AC}$ = 8.5 A/mm$^2$) waveforms.

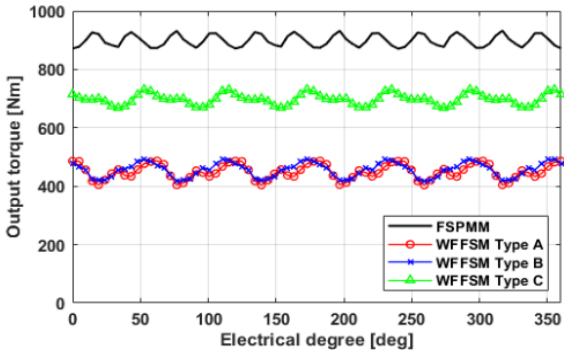


Fig. 12. Instantaneous torque waveforms for an electrical cycle (@ 4,000 rpm, $J_{DC}$ = 8.5 A/mm$^2$, and $J_{AC}$ = 8.5 A/mm$^2$).

TABLE 6. ELECTROMAGNETIC PERFORMANCE OF THE FSPMM AND WFFSMS AT RATED CONDITION (@ 4,000 rpm, $J_{DC}$ = 8.5 A/mm$^2$, and $J_{AC}$ = 8.5 A/mm$^2$).

| Machine | FSPMM | Type A | Type B | Type C |
|---|---|---|---|---|
| **Power (KW)** | 380.3 | 188.5 | 190.6 | 296.1 |
| **Torque [Nm]** | 908 | 450 | 455 | 707 |
| **Torque ripple [%]** | 6.16 | 18.46 | 16.4 | 8.88 |
| **Cogging torque [Nm]** | 66 | 87 | 84 | 89 |
| **Efficiency [%]** | 93 | 89 | 89.5 | 91 |

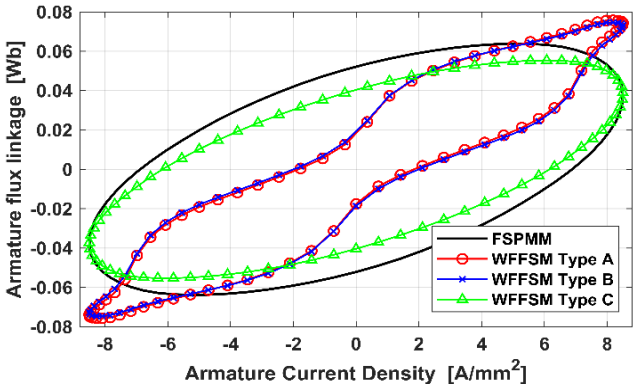


Fig. 13. Energy conversion loop of all FSMs (@ 4,000 RPM, $J_{DC}$ = 8.5 A/mm$^2$, and $J_{AC}$= 8.5 A/mm$^2$).

Hence, besides 12/10, the 12/11, 12/13, and 12/14 stator-rotor pole combinations are also viable. The terminal voltage along with armature winding self-inductance behavior over one electrical cycle for Type A with different pole combinations is shown in Fig. 14. Type A with an even number of rotor poles, i.e., 12/10 and 12/14, exhibits four distinct spikes in their terminal voltage and self-inductance profile at the same rotor positions. While Type A, featuring an odd number of rotor poles, i.e., 12/11 and 12/13, showcases two prominent spikes in their terminal voltage and self-inductance profile at the same rotor positions. It indicates that within one electrical cycle, for Type A with an odd number of rotor poles, i.e., 12/11 and 12/13, two particular rotor positions exist where a longer magnetic flux path is formed through the pole following the adjacent stator and rotor poles. Type A and Type B show the same behavior for terminal voltage and the self-inductance for different stator-rotor pole combinations.

The spectral analysis of the terminal voltage for various pole combinations in Type A is presented in Fig. 15. For more clarity and ease of scaling, the voltage values are normalized based on the maximum value of the fundamental component of the 12/10 combination (308.5 V). It is evident that 12/10 and 12/14 show a significant component of the 5$^{th}$, 7$^{th}$, 11$^{th}$, and 13$^{th}$ harmonics orders, while for 12/11 and 12/13, noticeable components include the 3$^{rd}$, 5$^{th}$, 7$^{th}$, 9$^{th,}$ and 11$^{th}$ harmonic orders.

The number of spikes in terminal voltage and self-inductance waveforms are summarized in Table 7. It indicates that the spikes in terminal voltage and self- and mutual inductances are attributed to the bridge structure and pole combination. For example, in the 12/10 combination and given stator and rotor tooth width, four rotor positions for each phase align stator and rotor teeth in a way that creates an additional magnetic flux path

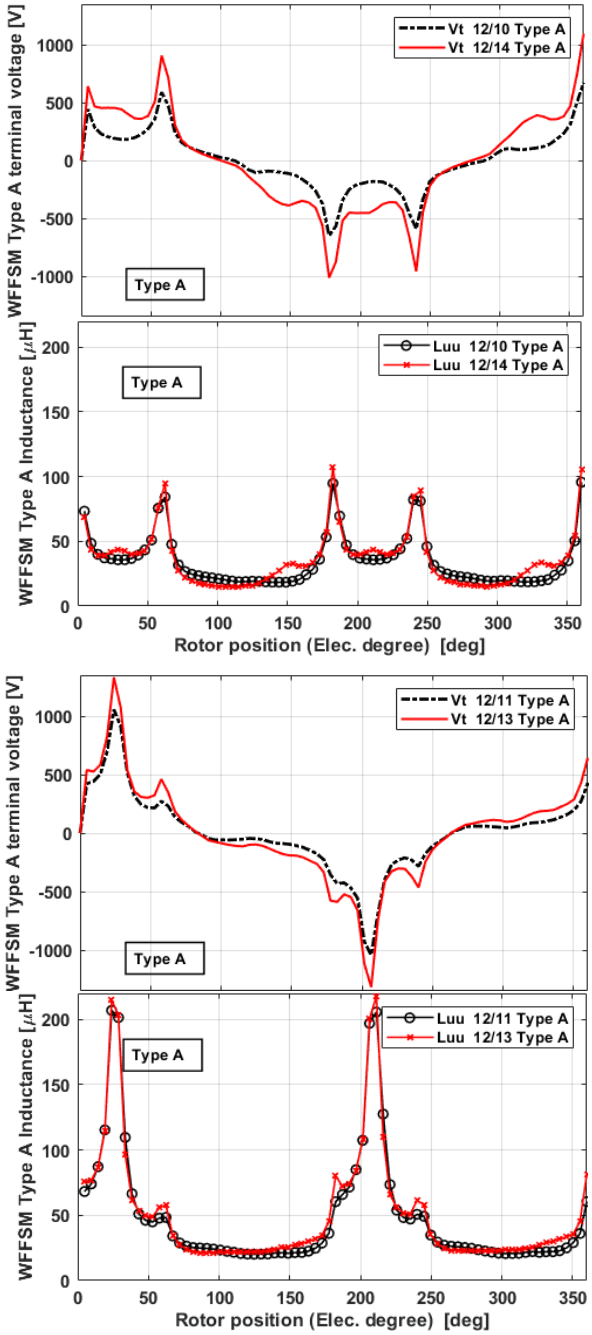


Fig. 14. Type A terminal voltage and self-inductance waveform for different stator-rotor pole combinations (@ 4,000 rpm, $J_{DC}$ = 8.5 A/mm$^2$, $J_{AC}$ = 8.5 A/mm$^2$).

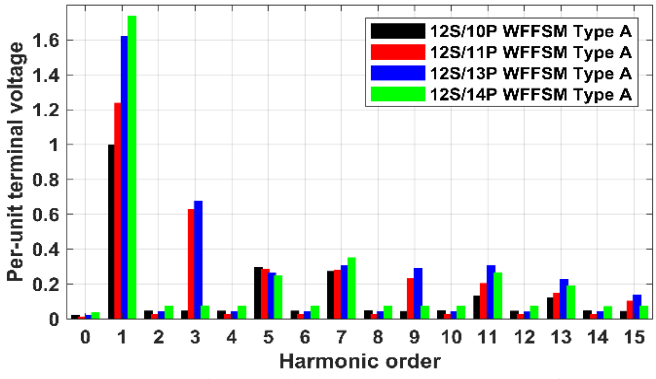


Fig. 15. Per-unit terminal voltage harmonics content of Type A (@ 4,000 rpm, $J_{DC}$ = 8.5 A/mm$^2$, $J_{AC}$= 8.5 A/mm$^2$).

TABLE 7. NUMBER OF VOLTAGE SPIKES IN ONE ELECTRIC CYCLE FOR WFFSM TYPE A AND TYPE B WITH DIFFERENT STATOR-ROTOR POLE COMBINATIONS

| Stator-Rotor pole combination | 12/10 | 12/11 | 12/13 | 12/14 |
|---|---|---|---|---|
| Number of spikes in terminal voltage waveform | 4 | 2 | 2 | 4 |
| Number of spikes in armature winding self-inductance waveform | 4 | 2 | 2 | 4 |

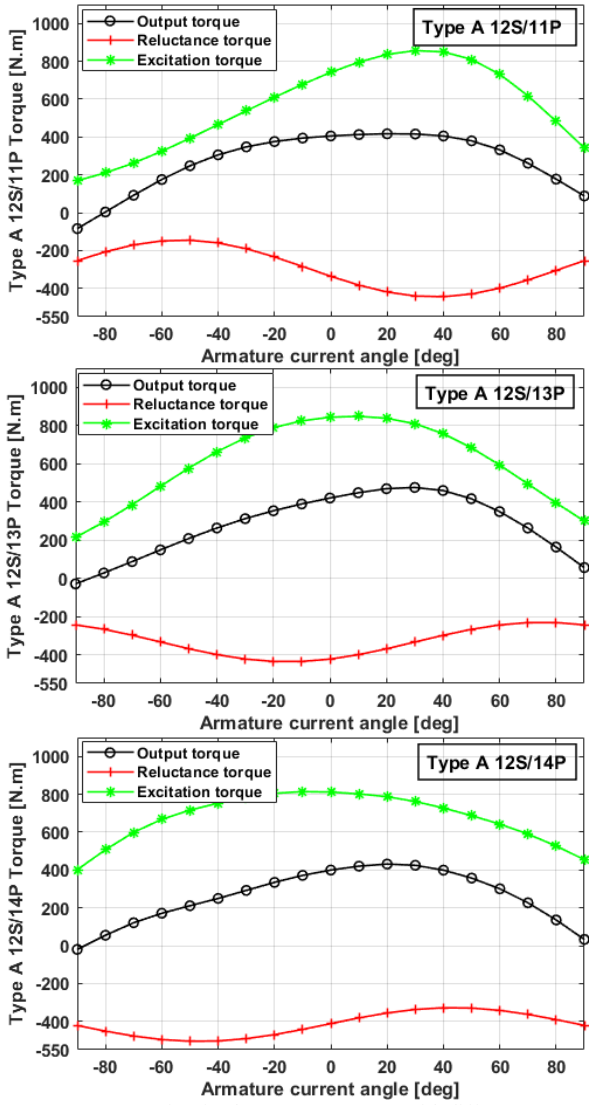


Fig. 16. Torque segregation for the WFFSM Type A with different stator-rotor pole combinations.

through the bridge, effectively creating a short circuit path for magnetic flux. This leads to a 100% increase in the average of both self- and mutual inductance and a 63% increase in terminal voltage rms value in Type A and Type B compared to that of FSPMM. The FEA results shows that for overload conditions, armature current density higher than 8.5 A/mm$^2$, the spikes in inductance and terminal voltage waveforms become more pronounced and visible. Consequently, the average value of self- and mutual inductances and also the rms value of terminal voltage increase. Additionally, the stator back iron and bridge experience increased saturation during overload conditions.

The torque components of the Type A, including excitation torque, reluctance torque, and net output torque, are plotted as functions of the armature current angle for different stator-rotor pole combinations in Fig. 16. A negative reluctance torque is generated at zero current angle. This negative reluctance torque arising from a substantial presence of self-inductance odd harmonics adversely affects the torque capability of the machine. It observed that the armature current angle for achieving maximum output torque is 20 degrees for all combinations.

## V. CONCLUSIONS

This paper proposed a multi-segment MEC analysis method to provide a better understanding of the magnetic flux path of FSPMM and WFFSMs with different winding configurations and stator-rotor pole combinations. It showed how the MMFs associated with armature winding currents interact with MMFs associated with excitation systems. The magnetic flux path analysis visually shows the difference in flux circulation paths in the integrated stator structure of the WFFSMs (i.e., longer and inefficient flux path). Due to the stator bridge structure, the longer magnetic flux path between stator poles generates localized saturation regions in the stator back iron and bridges. The integrated structure of WFFSMs causes terminal voltage, self- and mutual inductances to spike in some specific rotor positions during one electrical cycle. The number and location of these spikes depend on the rotor and stator geometry and the stator-rotor pole combinations. The odd order harmonics of inductances cause a negative reluctance torque, which decreases the net output torque.

The results demonstrate that the WFFSM employs a circumferential field and armature winding configuration, which avoids the longer magnetic flux path, shows promising electromagnetic performance and achieves the highest output torque. It exhibits an output torque that is 57% higher compared to WFFSMs afflicted by the longer magnetic flux path, with identical volume. The investigation of these different topologies will be continued in terms of geometry optimization, thermal management, efficiency, and manufacturing challenges.

## VI. REFERENCES

[1] "BMW's Magnet-Less Motor: How Does It Work?," MotorTrend, Jan. 13, 2022. https://www.motortrend.com/ news/bmw-ix-m60-brushed-electric-motor-tech-deep-dive/

[2] "ZF makes magnet-free electric motor uniquely compact and competitive - ZF," Zf.com, Sep. 2023. https://press.zf.com/press /en/releases /release_60480.html

[3] "MAHLE develops highly efficient magnet-free electric motor - MAHLE Newsroom," Mahle.com, 2022. https://newsroom.mahle.com/press/en/ press-releases/mahle-develops-highly-efficient-magnet-free-electric-motor--82368# (accessed Mar. 14, 2024).

[4] Z. Q. Zhu and X. Liu, "Novel Stator Electrically Field Excited Synchronous Machines Without Rare-Earth Magnet," *IEEE Trans. Magn.*, vol. 51, no. 4, pp. 1-9, April 2015.

[5] A. S. Thomas, Z. Q. Zhu, R. L. Owen, G. W. Jewell and D. Howe, "Multiphase flux-switching permanent-magnet brushless machine for aerospace application," *IEEE Trans. Ind. Appl.,* vol. 45, pp. 1971-1981, Nov. 2009.

[6] Y. J. Zhou and Z. Q. Zhu, "Comparison of wound-field switched-flux machines," *IEEE Trans. Ind. Appl,* vol. 50, no. 5, pp. 3314-3324, 2014.

[7] E. B. Sulaiman, T. Kosaka and N. Matsui, "Design study and experimental analysis of wound field flux switching motor for HEV applications," *XXth Int. Conf. on Elec. Mach.*, pp. 1269-1275,2012.

[8] G. Zhang, W. Hua, M. Tong and M. Cheng, "Design and manufacturing considerations of flux-switching permanent magnet motors for mass productions used in EVs and HEVs," *2015 18th International Conference on Electrical Machines and Systems (ICEMS)*, Pattaya, Thailand, 2015, pp. 1757-1763.

[9] M. Fereydoonian, D. Bobba, and W. Lee, "Magnetic flux path and inductance analysis of flux-switching machines with different field and armature winding configurations," in *Proc. IEEE Energy Convers. Cong. and Expo. (ECCE)*, 2022, pp. 1-6.

[10] M. Fereydoonian, K. Lee, D. Bobba, and W. Lee, "Comparative analysis of wound-field flux-switching machines with different field and armature winding configurations," *in proc. 2022 IEEE Transp. Electrific. Conf. & Expo. (ITEC), 2022, pp. 1076-1081.*

[11] M. Fereydoonian, K. Lee, G. Choi, and W. Lee, "Rotor Saliency Optimization for High-Power Density Wound-Field Flux-Switching Machines," *in Proc. IEEE Energy Convers. Cong. and Expo. (ECCE)*, Nashville, TN, USA, 2023, pp. 3867-3874.

[12] M. F. Omar, E. Sulaiman, M. Jenal, R. Kumar and R. N. Firdaus, "Magnetic Flux Analysis of a New Field-Excitation Flux Switching Motor Using Segmental Rotor," *IEEE Trans. on Magn.*, vol. 53, no. 11, pp. 1-4, Nov. 2017.

[13] C. Yu, S. Niu, S. L. Ho and W. N. Fu, "Magnetic Circuit Analysis for a Magnetless Double-Rotor Flux Switching Motor," *IEEE Trans. on Magn.*, vol. 51, no. 11, pp. 1-5, Nov. 2015.

[14] Z. Chen and Y. Cui, "Numerical Simulation and Experimental Validation of a Flux Switching Permanent Magnet Memory Machine," *IEEE Access*, vol. 8, pp. 194904-194911, 2020.

[15] Z. Q. Zhu, Y. Pang, D. Howe, S. Iwasaki, R. Deodhar and A. Pride, "Analysis of electromagnetic performance of flux-switching permanent-magnet Machines by nonlinear adaptive lumped parameter magnetic circuit model," *IEEE Trans. Magn*., vol. 41, no. 11, pp. 4277-4287, Nov. 2005.

[16] Y. Tang, J. J. H. Paulides and E. A. Lomonova, "Automated Design of DC-Excited Flux-Switching In-Wheel Motor Using Magnetic Equivalent Circuits," *IEEE Trans. Magn*., vol. 51, no. 4, pp. 1-11, April 2015, Art no. 8103411.

[17] Y. Tang, T. E. Motoasca, J. J. H. Paulides and E. A. Lomonova, "Analytical modeling of flux-switching machines using variable global reluctance networks," *XXth Int. Conf. on Elec. Mach.*, Marseille, France, 2012, pp. 2792-2798.

[18] J. D. McFarland, T. M. Jahns and A. M. El-Refaie, "Demagnetization performance characteristics of flux switching permanent magnet machines," *2014 Int. Conf. on Elect. Mach. (ICEM)*, Berlin, Germany, 2014, pp. 2001-2007.

[19] P. Naderi, S. Sharouni and M. Heidary, "A Novel Analysis on a New DC-Excited Flux-Switching Machine Using Modified MEC Method for Ground Power Unit Application," *IEEE Trans. Energy Convers.,* vol. 35, no. 4, pp. 1907-1915, Dec. 2020.

[20] X. Li, F. Shen, S. Yu and Z. Xue, "Flux-Regulation Principle and Performance Analysis of a Novel Axial Partitioned Stator Hybrid-Excitation Flux-Switching Machine Using Parallel Magnetic Circuit," *IEEE Trans. Ind. Electron.*, vol. 68, no. 8, pp. 6560-6573, Aug. 2021.

[21] J. H. Kim, Y. Li, D. Bobba and B. Sarlioglu, "Closed-Form Solutions Using Offset Angle for Winding Configurations of Flux-Switching Permanent Magnet Machines," *IEEE Trans. Ind. Appl.*, vol. 54, no. 4, pp. 3226-3234, July-Aug. 2018.

[22] M. Ibrahim and P. Pillay, "Aligning the Reluctance and Magnet Torque in Permanent Magnet Synchronous Motors for Improved Performance," *2018 IEEE Energy Conversion Congress and Exposition (ECCE)*, Portland, OR, USA, 2018, pp. 2286-2291.

[23] Y. Tang, J. J. H. Paulides, and E. A. Lomonova, "Energy conversion in dc excited flux-switching machines," *IEEE Trans. Magn.,* vol. 50, no. 11, pp. 1-4, Nov. 2014.

[24] U. B. Akuru and M. J. Kamper, "Formulation and Multiobjective Design Optimization of Wound-Field Flux Switching Machines for Wind Energy Drives," *IEEE Trans. Ind. Electron*., vol. 65, no. 2, pp. 1828-1836, Feb. 2018.

[25] W. Wang, Y. Wang, E. Ma and L. Wu, "Optimal Designs of Wound Field Switched Flux Machines with Different DC Windings Configurations," *CES Trans. Elec. Mach. and Syst.*, vol. 6, no. 4, pp. 359-367, December 2022.

[26] W. Zhang et al., "Reduction of Open-Circuit DC Winding Induced Voltage and Torque Pulsation in the Wound Field Switched Flux Machine by Stator Axial Pairing of Tooth Tips," *IEEE Trans. Ind. Appl*, vol. 58, no. 2, pp. 1976-1990, March-April 2022.

[27] W. Zhang, W. Hua, Z. Wu, G. Zhao, Y. Wang and W. Xia, "Analysis of DC Winding Induced Voltage in Wound-Field Flux-Switching Machine With Air-Gap Field Modulation Principle," *IEEE Trans. Ind. Electron*., vol. 69, no. 3, pp. 2300-2311, March 2022.

[28] W. Jiang, W. Huang, X. Lin, Y. Zhao and S. Zhu, "Analysis of Rotor Poles and Armature Winding Configurations Combinations of Wound Field Flux Switching Machines," *IEEE Trans. Ind. Electron.*, vol. 68, no. 9, pp. 7838-7849, Sept. 2021.

[29] X. Jiang, G. Zhao, W. Hua, S. Ding, Z. Chang and Y. Dai, "A Novel Multi-Excitation-Tooth Non-overlapping Stator Wound Field Synchronous Machine With Salient Rotor," in *IEEE Access*, vol. 10, pp. 69125-69134, 2022.

[30] Z. Wu et al., "Analysis and Suppression of Induced Voltage Pulsation in DC Winding of Five-Phase Wound-Field Switched Flux Machines," *IEEE Trans. Energy Convers.*, vol. 34, no. 4, pp. 1890-1905, Dec. 2019,

[31] A. Lindner and I. Hahn, "Simulation of a toroidal wound flux-switching permanent magnet machine," *IECON 2014 - 40th Annu. Conf. of the IEEE Ind. Electron. Soc*., 2014.

[32] M. Liu, Y. Li and B. Sarlioglu, "Thermal analysis of a novel dual-stator 6/4 flux-switching permanent magnet machine," 2017 *IEEE Power & Energy Society General Meeting*, Chicago, IL, USA, 2017, pp. 1-5,

[33] A. Zulu, "Flux switching machines using segmental rotors," Ph.D. dissertation, School of Elec. Electron. and Comput. Eng., Newcastle Univ., Newcastle, UK, 2010.

[34] Y. Tang, E. Ilhan, J. H. Paulides and E. A. Lomonova, "Design considerations of flux-switching machines with permanent magnet or DC excitation," *15th Eur. Conf. on Power Electron. and Appl.* (EPE), Lille, France, 2013, pp. 1-10.

[35] L. Shao, W. Hua, N. Dai, M. Tong, and M. Cheng, "Mathematical modeling of a 12-phase flux-switching permanent-magnet machine for wind power generation," *IEEE Trans. Ind. Electron.*, vol. 63, no. 1, pp. 504-516, Jan. 2016.

[36] E. Ilhan, M. F. J. Kremers, E. T. Motoasca, J. J. H. Paulides, and E. A. Lomonova, "Sensitivity analysis for phase inductances in flux-switching pm machines," in *proc. 2012 XXth Int. Conf. on Elect. Mach.*, 2012.

[37] W. Hua and C. Ming, "Inductance characteristics of 3-phase flux-switching permanent magnet machine with doubly-salient structure," in *proc. 2006 CES/IEEE 5th Int. Power Electron. and Motion Control Conf.*, 2006.

[38] T. Sun, S. Kwon, S. Lee, and J. Hong, "Investigation and comparison of inductance calculation methods in interior permanent magnet synchronous motors," in *proc. 2008 Int. Conf. on Elect. Mach. and Syst.*, 2008. pp. 3131-3136.

[39] M. Mabhula, U. B. Akuru, and M. J. Kamper, "Cross-coupling inductance parameter estimation for more accurate performance evaluation of wound-field flux modulation machines," *Electron.*, vol. 9, no. 11, p. 1748, Oct. 2020.

[40] Y. Tang, J. H. Paulides and E. A. Lomonova, "Field weakening performance of flux-switching machines for hybrid/electric vehicles," 2015 *Tenth Int. Conf. on Ecological Vehicles and Renewable Energies (EVER)*, pp. 1-10.

[41] L. R. Huang, J. H. Feng, S. Y. Guo, Y. F. Li, J. X. Shi and Z. Q. Zhu, "Rotor Shaping Method for Torque Ripple Mitigation in Variable Flux Reluctance Machines," in *IEEE Trans. Energy Convers.*, Sept. vol. 33, no. 3, pp. 1579-1589, 2018.

[42] J. T. Chen and Z. Q. Zhu, "Winding Configurations and Optimal Stator and Rotor Pole Combination of Flux-Switching PM Brushless AC Machines," *IEEE Trans. Energy Convers*., vol. 25, no. 2, pp. 293-302, June 2010.